

SHOCKS AND SPATIALLY OFFSET ACTIVE GALACTIC NUCLEI PRODUCE VELOCITY OFFSETS IN EMISSION LINES

JULIA M. COMERFORD¹, R. SCOTT BARROWS¹, JENNY E. GREENE², AND DAVID POOLEY³
¹Department of Astrophysical and Planetary Sciences, University of Colorado, Boulder, CO 80309, USA
²Department of Astrophysical Sciences, Princeton University, Princeton, NJ 08544, USA and
³Department of Physics and Astronomy, Trinity University, San Antonio, TX 78212, USA

Published in ApJ

ABSTRACT

While 2% of active galactic nuclei (AGNs) exhibit narrow emission lines with line-of-sight velocities that are significantly offset from the velocity of the host galaxy's stars, the nature of these velocity offsets is unknown. We investigate this question with *Chandra*/ACIS and *Hubble Space Telescope*/Wide Field Camera 3 observations of seven velocity-offset AGNs at $z < 0.12$, and all seven galaxies have a central AGN but a peak in emission that is spatially offset by < 1 kpc from the host galaxy's stellar centroid. These spatial offsets are responsible for the observed velocity offsets and are due to shocks, either from AGN outflows (in four galaxies) or gas inflowing along a bar (in three galaxies). We compare our results to a velocity-offset AGN whose velocity offset originates from a spatially offset AGN in a galaxy merger. The optical line flux ratios of the offset AGN are consistent with pure photoionization, while the optical line flux ratios of our sample are consistent with contributions from photoionization and shocks. We conclude that these optical line flux ratios could be efficient for separating velocity-offset AGNs into subgroups of offset AGNs – which are important for studies of AGN fueling in galaxy mergers – and central AGNs with shocks – where the outflows are biased towards the most energetic outflows that are the strongest drivers of feedback.

Subject headings: galaxies: active – galaxies: interactions – galaxies: nuclei

1. INTRODUCTION

Galaxies and their supermassive black holes are linked in their evolution, resulting in surprisingly tight observational correlations between parameters such as supermassive black hole mass, stellar velocity dispersion, and host galaxy mass (Heckman & Best 2014 for a review). Active galactic nuclei (AGNs) have emerged as key players in this coevolution, by the primary mechanisms of AGN fueling and AGN feedback. Supermassive black holes build up mass by accreting gas during AGN fueling, while AGN outflows are a crucial regulator of star formation that controls the mass growth of the galaxies (e.g., Di Matteo et al. 2005; Croton et al. 2006; Fabian 2012).

In recent years, double-peaked narrow emission lines in AGN host galaxies have been studied as a population (e.g., Liu et al. 2010; Comerford et al. 2011; Barrows et al. 2012; Comerford et al. 2012; Fu et al. 2012; Barrows et al. 2013; McGurk et al. 2015), and have been shown to be signatures of both AGN fueling and AGN outflows. Some of these double-peaked emission lines are produced by dual AGNs, which are a pair of AGNs being fueled during a galaxy merger (Fu et al. 2011; Liu et al. 2013; Comerford et al. 2015; Müller-Sánchez et al. 2015), and the majority of double-peaked emission lines are produced by AGN outflows (e.g., Rosario et al. 2010a; Greene et al. 2012; Nevin et al. 2016).

Analogous to the AGNs with double-peaked narrow emission lines, there is also a population of galaxy spectra with single-peaked narrow AGN emission lines that exhibit a statistically significant line-of-sight velocity offset relative to the velocity of the host galaxy's stars; 2% of AGNs exhibit these velocity offsets (Comerford et al. 2009, 2013). These objects have been much less well

studied than the AGNs with double-peaked narrow emission lines, and numerical simulations of galaxy mergers show that velocity-offset emission lines can be produced by offset AGNs, which are off-nuclear AGNs in ongoing galaxy mergers (e.g., Blecha et al. 2013; Steinborn et al. 2016). Inflows or outflows of gas could also produce velocity-offset AGN emission lines (e.g., Allen et al. 2015).

Here, we investigate the origins of the velocity-offset narrow emission lines observed in the Sloan Digital Sky Survey (SDSS) spectra of seven AGNs at $z < 0.12$. We observe each galaxy with the *Chandra X-ray Observatory* ACIS (*Chandra*/ACIS), to pinpoint the location of the AGN, and the *Hubble Space Telescope* Wide Field Camera 3 (*HST*/WFC3), to obtain high spatial resolution maps of the stellar continuum and the ionized gas. Our goal is to determine the nature of each galaxy and whether its velocity-offset emission lines are tracers of AGN fueling (via inflows or offset AGNs) or AGN feedback (via outflows).

This paper is organized as follows: In Section 2 we describe the sample selection and characteristics. In Section 3 we describe the observations of the sample (SDSS spectra, Keck/OSIRIS integral-field spectroscopy for three of the seven galaxies, *Chandra* observations, and *HST*/WFC3 multiband imaging), the astrometry, and our analyses of the data. Section 4 presents our results, including the nature of each velocity-offset AGN. Finally, our conclusions are summarized in Section 5.

We assume a Hubble constant $H_0 = 70$ km s⁻¹ Mpc⁻¹, $\Omega_m = 0.3$, and $\Omega_\Lambda = 0.7$ throughout, and all distances are given in physical (not comoving) units.

2. THE SAMPLE

We begin with a parent sample of 18,314 Type 2 AGNs at $z < 0.21$ in SDSS, which were identified as AGNs via their optical emission line ratios (Brinchmann et al. 2004) and the requirement that the fits to the absorption and emission line systems in the SDSS spectra are robust (by examining the signal, residual noise, and statistical noise; Oh et al. 2011). The line-of-sight velocity offsets of the emission lines relative to the stellar absorption lines were then measured. From the parent sample of 18,314 Type 2 AGNs, the velocity-offset AGNs were the systems that fulfilled the following four criteria: 1) the velocity offsets of the forbidden emission lines and the Balmer emission lines are the same to within 1σ ; 2) the velocity offsets of the emission lines are greater than 3σ in significance; 3) the emission line profiles are symmetric; 4) the systems do not have double-peaked emission lines.

The 351 AGNs that meet these criteria are the velocity-offset AGNs (Comerford & Greene 2014). From these 351 velocity-offset AGNs, we select seven systems with low redshifts ($z < 0.12$) and high estimated 2-10 keV fluxes ($> 5 \times 10^{-14}$ erg cm $^{-2}$ s $^{-1}$). We estimate the 2-10 keV fluxes from the [O III] $\lambda 5007$ fluxes of the AGNs (which are $> 1.3 \times 10^{-14}$ erg cm $^{-2}$ s $^{-1}$ for this sample of seven systems) and the established Type 2 AGN [O III] $\lambda 5007$ to X-ray scaling relation (Heckman et al. 2005). The low redshifts maximize the physical spatial resolution that we can achieve with *Chandra* and *HST*, while the high 2-10 keV fluxes minimize the observing time necessary for X-ray detections. The seven systems are listed in Table 1.

3. OBSERVATIONS AND ANALYSIS

3.1. Optical SDSS Observations

For each of the seven velocity-offset AGNs, the host galaxy redshift (based on the stellar absorption features), the line-of-sight velocity offset of the emission lines, and the [O III] $\lambda 5007$ luminosity were determined from the SDSS spectrum (Comerford & Greene 2014). Three of the AGNs have emission lines with redshifted velocity offsets, and four have emission lines with blueshifted velocity offsets. The absolute values of the velocity offsets range from 50 to 113 km s $^{-1}$ (Table 1).

3.2. Keck/OSIRIS Near-infrared IFU Observations

Three of the velocity-offset AGNs were observed with Keck Laser Guide Star Adaptive Optics with OH-Suppressing Infra-Red Imaging Spectrograph (OSIRIS) integral-field spectroscopy (Müller-Sánchez et al. 2016). In each galaxy (SDSS J1055+1520, SDSS J1117+6140, and SDSS J1346+5228), the peak of the line emission (Pa α , Pa α , and [Fe II] in each galaxy, respectively) was spatially offset from the galaxy center by 0''.1 (0.2 kpc), 0''.2 (0.5 kpc), and 0''.3 (0.2 kpc), respectively. Based on the kinematics of the gas in the OSIRIS observations, Müller-Sánchez et al. (2016) found that SDSS J1055+1520 and SDSS J1346+5228 host AGN outflows while SDSS J1117+6140 has gas inflow along a bar. They concluded that the spatially-offset peaks in line emission are the result of the outflows or inflows driving shocks into off-nuclear gas.

3.3. Chandra/ACIS X-ray Observations

The seven velocity-offset AGNs were observed with *Chandra*/ACIS for the program GO4-15113X (PI: Comerford). Our exposure times were derived from the observed [O III] $\lambda 5007$ flux for each system (Table 1) and the scaling relation between [O III] $\lambda 5007$ flux and hard X-ray (2-10 keV) flux for Type 2 AGNs, which has a scatter of 1.06 dex (Heckman et al. 2005). We selected exposure times that would ensure a firm detection of at least 10 counts for each AGN, even in the case of the actual X-ray flux falling in the low end of the 1.06 dex scatter. The galaxies were observed with exposure times of 10 ks to 20 ks (Table 2).

The galaxies were observed with the telescope aim-point on the ACIS S3 chip in “timed exposure” mode and telemetered to the ground in “faint” mode. We reduced the data with the latest *Chandra* software (CIAO 4.6.1) in combination with the most recent set of calibration files (CALDB 4.6.2).

For each galaxy, we used *dmcopy* to make a sky image of the field in the rest-frame soft (0.5–2 keV), hard (2–10 keV) and total (0.5–10 keV) energy ranges. Using the modeling facilities in *Sherpa*, we simultaneously modeled the source as a two-dimensional Lorentzian function (`beta2d`: $f(r) = A(1 + [r/r_0]^2) - \alpha$) and the background as a fixed count rate estimated using a source-free adjacent circular region of 30'' radius. We used the SDSS galaxy coordinates as the initial position of the `beta2d` component, and then we allowed the model to fit a region of 3 times the PSF size (estimated with `psfSize`) at that location. We determined the best-fit model parameters with *Sherpa*'s implementation of the ‘Simplex’ minimization algorithm (Lagarias et al. 1998), by minimizing the Cash statistic. We also attempted a two-component `beta2d` model to test for additional sources, but all secondary components were detected with $< 1\sigma$ significance. Therefore, none of the systems require a secondary component, and Table 3 and Figure 1 show the best-fit positions of the X-ray source in each galaxy. Table 3 also gives the spatial separations between each X-ray source and the host galaxy’s stellar nucleus. The errors on these separations are dominated by the astrometric uncertainties in aligning the *Chandra* and *HST* images. These astrometric errors are calculated in Section 3.5, and the median astrometric error is 0''.5.

Then, we used the Bayesian Estimation of Hardness Ratios (BEHR) code (Park et al. 2006) to measure the rest-frame soft, hard, and total counts in each X-ray source. We used `calc_data_sum` to determine the number of observed soft and hard counts from both the source region and a background region, and then BEHR used a Bayesian approach to estimate the expected values and uncertainties of the rest-frame soft counts, hard counts, total counts, and hardness ratio. Table 4 shows these values, and we estimated errors on the counts assuming Poisson noise.

To model the energy spectra of the extracted regions over the observed energy range 2-8 keV, we used *Sherpa*. We fit each unbinned spectrum with a redshifted power law, $F \sim E^{-\Gamma}$ (which represents the intrinsic AGN X-ray emission at the SDSS spectroscopic redshift z). This spectrum is attenuated by passing through two absorbing column densities of neutral Hydrogen. One of these is fixed to the Galactic value, $n_{H,Gal}$, and the other is assumed to be intrinsic to the source, $n_{H,exgal}$, at the

TABLE 1
MEASUREMENTS FROM SDSS OBSERVATIONS

SDSS Designation	z	Δv (km s ⁻¹)	$L_{[\text{O III}]\lambda 5007}$ (10 ⁴⁰ erg s ⁻¹)
SDSS J013258.92-102707.0	0.03222 ± 0.00002	56 ± 10	5.5 ± 0.6
SDSS J083902.97+470756.3	0.05236 ± 0.00006	-50 ± 10	17.7 ± 1.2
SDSS J105553.64+152027.4	0.09201 ± 0.00002	-113 ± 10	48.1 ± 5.7
SDSS J111729.22+614015.2	0.11193 ± 0.00001	85 ± 12	44.5 ± 7.2
SDSS J134640.79+522836.6	0.02918 ± 0.00001	-52 ± 10	7.5 ± 0.8
SDSS J165430.72+194615.5	0.05367 ± 0.00001	66 ± 11	20.7 ± 2.8
SDSS J232328.01+140530.2	0.04142 ± 0.00007	-53 ± 10	10.2 ± 1.3

NOTE. — Column 2: host galaxy redshift, based on stellar absorption features. Column 3: line-of-sight velocity offset of emission lines relative to host galaxy systemic. Column 4: observed [O III] $\lambda 5007$ luminosity.

TABLE 2
SUMMARY OF CHANDRA AND HST OBSERVATIONS

SDSS Name	<i>Chandra</i> /ACIS exp. time (s)	<i>Chandra</i> /ACIS obs. date (UT)	<i>HST</i> /WFC3 F160W exp. time (s)	<i>HST</i> /WFC3 F606W exp. time (s)	<i>HST</i> /WFC3 F438W exp. time (s)	<i>HST</i> /WFC3 obs. date (UT)
J0132-1027	14871	2014-08-23	147	900	1047	2014-06-24
J0839+4707	9927	2014-09-03	147	945	1050	2014-09-06
J1055+1520	14869	2015-02-04	147	900	957	2014-10-25
J1117+6140	19773	2015-02-03	147	1062	1065	2014-07-03
J1346+5228	9937	2014-08-29	147	996	1050	2015-02-05
J1654+1946	9937	2014-07-23	147	900	957	2014-07-27
J2323+1405	14868	2014-08-31	147	900	954	2014-06-08

NOTE. — Column 2: exposure time for the *Chandra*/ACIS observation. Column 3: UT date of the *Chandra*/ACIS observation. Columns 4 – 6: exposure times for the *HST*/WFC3 F160W, F606W, and F438W observations. Column 7: UT date of the *HST*/WFC3 observations.

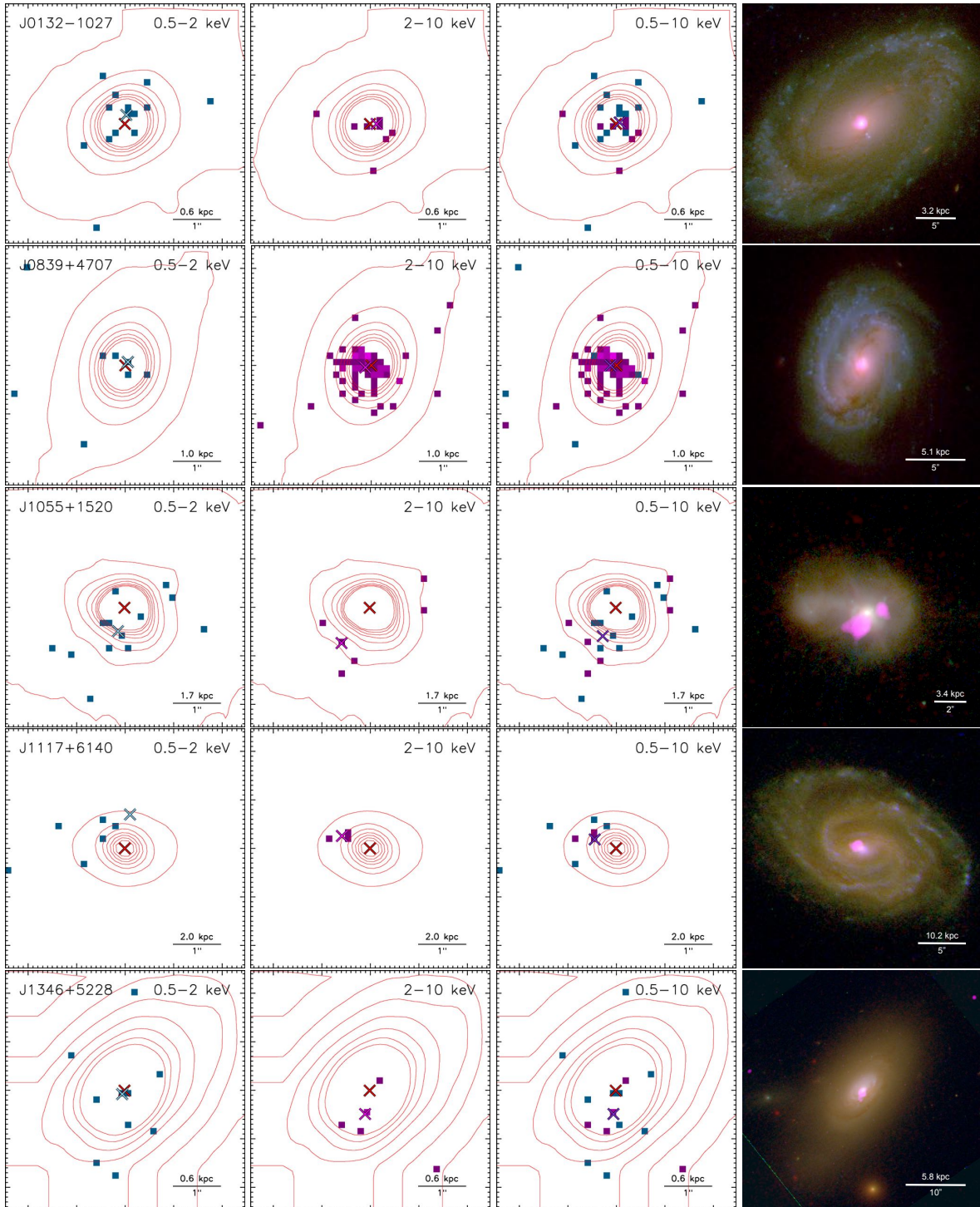
TABLE 3
CHANDRA AND HST/F160W POSITIONS OF EACH SOURCE

SDSS Name	RA _{<i>HST</i>/F160W}	DEC _{<i>HST</i>/F160W}	<i>Chandra</i> Energy Range (keV)	RA _{<i>Chandra</i>} ^a	DEC _{<i>Chandra</i>} ^a	$\Delta\theta$ ($''$) ^b	Δx (kpc) ^b	Sig.
J0132-1027	01:32:58.927	-10:27:07.05	0.5 – 2	01:32:58.924	-10:27:06.87	0.18 ± 0.33	0.12 ± 0.21	0.6 σ
			2 – 10	01:32:58.917	-10:27:07.05	0.14 ± 0.46	0.09 ± 0.29	0.3 σ
			0.5 – 10	01:32:58.922	-10:27:07.02	0.08 ± 0.43	0.05 ± 0.27	0.2 σ
J0839+4707	08:39:02.949	+47:07:55.88	0.5 – 2	08:39:02.944	+47:07:55.95	0.09 ± 0.29	0.09 ± 0.30	0.3 σ
			2 – 10	08:39:02.961	+47:07:55.84	0.13 ± 0.19	0.13 ± 0.19	0.7 σ
			0.5 – 10	08:39:02.961	+47:07:55.88	0.12 ± 0.18	0.12 ± 0.18	0.7 σ
J1055+1520	10:55:53.644	+15:20:27.87	0.5 – 2	10:55:53.653	+15:20:27.40	0.49 ± 0.84	0.83 ± 1.44	0.6 σ
			2 – 10	10:55:53.682	+15:20:27.16	0.90 ± 0.84	1.54 ± 1.44	1.1 σ
			0.5 – 10	10:55:53.662	+15:20:27.30	0.62 ± 0.84	1.07 ± 1.44	0.7 σ
J1117+6140	11:17:29.208	+61:40:15.38	0.5 – 2	11:17:29.193	+61:40:16.06	0.69 ± 0.73	1.41 ± 1.49	0.9 σ
			2 – 10	11:17:29.287	+61:40:15.63	0.62 ± 0.37	1.26 ± 0.76	1.7 σ
			0.5 – 10	11:17:29.268	+61:40:15.56	0.46 ± 0.36	0.94 ± 0.74	1.3 σ
J1346+5228	13:46:40.812	+52:28:36.22	0.5 – 2	13:46:40.816	+52:28:36.15	0.08 ± 0.36	0.05 ± 0.21	0.2 σ
			2 – 10	13:46:40.821	+52:28:35.76	0.48 ± 0.35	0.28 ± 0.20	1.4 σ
			0.5 – 10	13:46:40.816	+52:28:35.76	0.47 ± 0.35	0.27 ± 0.21	1.3 σ
J1654+1946	16:54:30.724	+19:46:15.56	0.5 – 2	16:54:30.734	+19:46:15.45	0.17 ± 0.48	0.18 ± 0.50	0.4 σ
			2 – 10	16:54:30.806	+19:46:15.78	1.17 ± 0.44	1.22 ± 0.46	2.6 σ
			0.5 – 10	16:54:30.732	+19:46:15.42	0.18 ± 0.44	0.18 ± 0.46	0.4 σ
J2323+1405	23:23:28.010	+14:05:30.08	0.5 – 2	23:23:27.996	+14:05:30.12	0.21 ± 0.26	0.17 ± 0.22	0.8 σ
			2 – 10	23:23:28.008	+14:05:30.12	0.05 ± 0.22	0.04 ± 0.18	0.2 σ
			0.5 – 10	23:23:28.003	+14:05:30.12	0.11 ± 0.21	0.09 ± 0.17	0.5 σ

NOTE. — Columns 2 and 3: coordinates of the host galaxy's stellar nucleus, measured from *HST*/WFC3/F160W observations. Column 4: rest-frame energy range of *Chandra* observations. Columns 5 and 6: coordinates of the X-ray AGN source, measured from *Chandra*/ACIS observations in the energy range given in Column 4. Columns 7 and 8: angular and physical separations between the positions of the host galaxy's stellar nucleus and the X-ray AGN source, where the error includes uncertainties in the positions of the *HST* and *Chandra* sources as well as the astrometric uncertainty. Column 9: significance of the separation between the host galaxy's stellar nucleus and the X-ray AGN source.

^a The astrometric shifts described in Section 3.5 have been applied to the *Chandra* source positions.

^b The errors are dominated by the astrometric uncertainties, which range from 0''.2 to 0''.8.



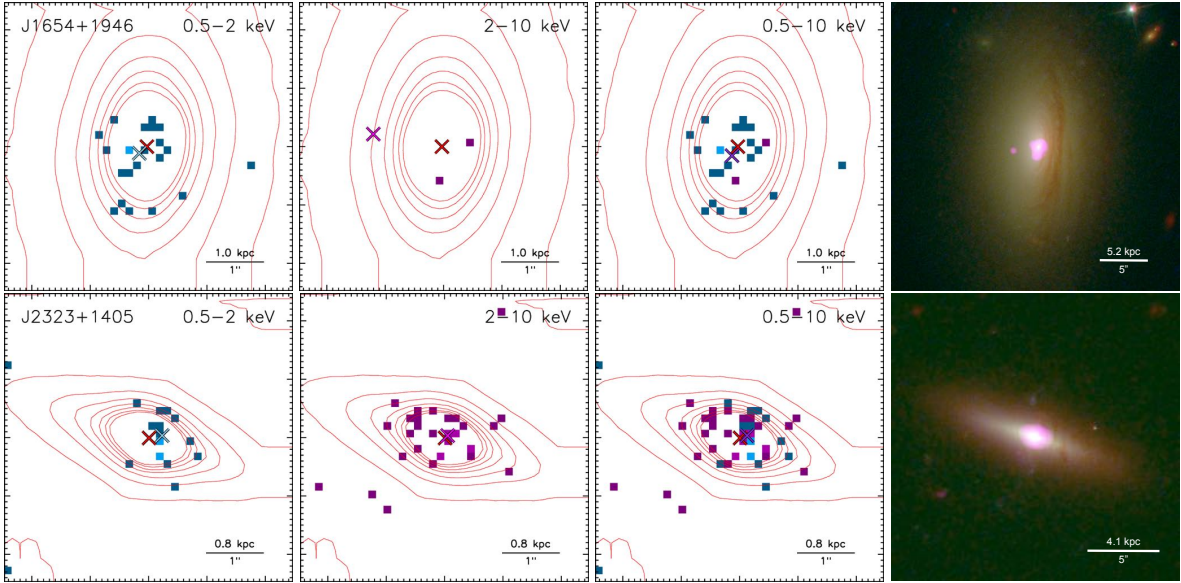


FIG. 1.— From left to right: *Chandra* restframe 0.5 – 2 keV (soft) observations, *Chandra* restframe 2 – 10 keV (hard) observations, *Chandra* restframe 0.5 – 10 keV (total) observations, and four-color combined *Chandra* and *HST* observations for each velocity-offset AGN. The leftmost three panels show $5'' \times 5''$ images centered on the host galaxy (red crosses indicate the centers of the host galaxies, based on *HST*/F160W observations). The red curves show linear contours for the *HST*/F160W observations. The pixels are one-fourth size *Chandra* pixels (soft X-rays shown in blue and hard X-rays shown in magenta), and the blue, magenta, and purple crosses indicate the best-fit locations of the soft, hard, and total X-ray sources, respectively. The rightmost panels show four-color images of *HST* F160W (red), F606W (green), F438W (blue), and *Chandra* restframe 0.5 – 10 keV (purple, one-twelfth size pixels smoothed with a 16 pixel radius Gaussian kernel) observations, where the *HST* and *Chandra* images have been aligned using the astrometric shifts described in Section 3.5. In all panels, north is up and east is to the left.

TABLE 4
X-RAY COUNTS AND SPECTRAL FITS

SDSS Name	Soft Counts (0.5 – 2 keV)	Hard Counts (2 – 10 keV)	Total Counts (0.5 – 10 keV)	Hardness Ratio	$n_{H,exgal}$ (10^{22} cm^{-2})	Γ	Reduced C-stat
J0132–1027	$14.9^{+3.1}_{-4.2}$	$8.2^{+2.3}_{-3.4}$	$23.1^{+4.2}_{-5.2}$	$-0.30^{+0.19}_{-0.22}$	< 0.02	$1.73^{+0.41}_{-0.38}$	0.24
J0839+4707	$8.7^{+2.1}_{-3.4}$	$66.1^{+7.4}_{-8.6}$	$74.8^{+7.9}_{-9.1}$	$0.77^{+0.09}_{-0.06}$	$8.18^{+2.21}_{-0.29}$	1.70 (fixed) ^a	0.59
J1055+1520	$15.8^{+3.2}_{-4.5}$	$6.8^{+2.0}_{-3.3}$	$22.7^{+4.1}_{-5.3}$	$-0.40^{+0.19}_{-0.22}$	< 0.03	$1.71^{+0.39}_{-0.47}$	0.22
J1117+6140	$7.6^{+2.0}_{-3.3}$	$3.1^{+1.1}_{-2.5}$	$10.7^{+2.6}_{-4.0}$	$-0.43^{+0.25}_{-0.35}$	< 0.10	$1.87^{+0.78}_{-0.76}$	0.12
J1346+5228	$10.8^{+2.4}_{-3.9}$	$7.2^{+1.9}_{-3.3}$	$18.0^{+3.8}_{-4.7}$	$-0.21^{+0.23}_{-0.25}$	< 0.12	$1.35^{+0.54}_{-0.85}$	0.19
J1654+1946	$23.9^{+4.2}_{-5.3}$	$4.2^{+1.4}_{-2.7}$	$28.1^{+6.0}_{-6.0}$	$-0.71^{+0.11}_{-0.17}$	< 0.02	1.70 (fixed) ^a	0.20
J2323+1405	$17.4^{+3.5}_{-4.7}$	$32.5^{+5.2}_{-6.2}$	$49.9^{+6.3}_{-7.6}$	$0.30^{+0.15}_{-0.13}$	$0.41^{+0.18}_{-0.16}$	1.70 (fixed) ^a	0.52

NOTE. — Column 2: soft X-ray (restframe 0.5-2 keV) counts (S). Column 3: hard X-ray (restframe 2-10 keV) counts (H). Column 4: total X-ray (restframe 0.5-10 keV) counts. Column 5: hardness ratio $HR = (H-S)/(H+S)$. Column 6: extragalactic column density. Column 7: best-fit spectral index. Column 8: reduced Cash statistic of the fit.

^a The best-fit spectrum had a spectral index of $\Gamma < 1$ or $\Gamma > 3$, so we redid the fit by freezing the spectral index to $\Gamma = 1.70$.

redshift z . We determined $n_{H,Gal}$ using an all-sky interpolation of the H I in the Galaxy (Dickey & Lockman 1990).

For our first fit to each spectrum, we allowed Γ and $n_{H,exgal}$ to vary freely. If the best-fit value of Γ was not within the typical range of observed power-law indices, i.e. $1 \leq \Gamma \leq 3$ (Ishibashi & Courvoisier 2010; Piconcelli et al. 2005; Nandra & Pounds 1994; Reeves & Turner 2000), then we fixed Γ at a value of 1.7, which is a typical value for the continuum of Seyfert galaxies, and ran the fit again.

To determine the best-fit model parameters for each spectrum, we used *Sherpa*'s implementation of the Levenberg-Marquardt optimization method (Bevington 1969) to minimize the Cash statistic. Table 4 shows the results of these spectral fits. All fluxes are k -corrected,

and we calculated the observed flux values from the model sum (including the absorbing components) and the intrinsic flux values from the unabsorbed power law component. Finally, we used the redshift to determine the distance to each system and convert the X-ray fluxes to X-ray luminosities (Table 5).

3.4. *HST*/WFC3 F438W, F606W, and F160W Observations

The seven velocity-offset AGNs were also observed with *HST*/WFC3 (GO 13513, PI: Comerford), and the observations covered three bands: UVIS/F438W (B band), UVIS/F606W (V band), and IR/F160W (H band). The exposure times are summarized in Table 2.

Each band revealed different properties of the galaxies. The F438W observations covered $H\delta$, $H\gamma$, and [O III] $\lambda 4363$ for the $0.02 < z < 0.06$ galax-

TABLE 5
 X-RAY LUMINOSITIES

SDSS Name	$L_{X,0.5-2\text{keV}}$ abs (unabs) (10^{40} erg s $^{-1}$)	$L_{X,2-10\text{keV}}$ abs (unabs) (10^{40} erg s $^{-1}$)	$L_{X,0.5-10\text{keV}}$ abs (unabs) (10^{40} erg s $^{-1}$)
J0132-1027	$1.2^{+0.4}_{-0.3}$ ($1.3^{+0.4}_{-0.4}$)	$2.3^{+2.1}_{-1.2}$ ($2.3^{+2.1}_{-1.2}$)	$3.3^{+2.5}_{-1.2}$ ($3.5^{+2.6}_{-1.3}$)
J0839+4707	$0.2^{+0.5}_{-0.1}$ ($89.7^{+29.6}_{-29.0}$)	$165.0^{+44.7}_{-37.6}$ ($245.0^{+61.2}_{-59.8}$)	$170.0^{+39.6}_{-40.1}$ ($338.0^{+83.0}_{-84.3}$)
J1055+1520	$9.7^{+3.2}_{-3.5}$ ($11.6^{+3.3}_{-3.8}$)	$18.4^{+19.2}_{-8.8}$ ($18.5^{+19.2}_{-8.8}$)	$30.1^{+22.5}_{-12.7}$ ($32.3^{+21.1}_{-13.3}$)
J1117+6140	$3.9^{+2.4}_{-1.9}$ ($6.4^{+2.5}_{-2.9}$)	$7.7^{+14.6}_{-5.1}$ ($7.8^{+14.6}_{-5.1}$)	$12.3^{+15.1}_{-7.1}$ ($14.9^{+14.0}_{-8.2}$)
J1346+5228	$0.8^{+0.4}_{-0.3}$ ($1.0^{+0.4}_{-0.4}$)	$2.7^{+3.1}_{-1.4}$ ($2.7^{+3.1}_{-1.5}$)	$3.7^{+3.5}_{-1.7}$ ($3.8^{+3.6}_{-1.7}$)
J1654+1946	$5.5^{+1.2}_{-1.2}$ ($6.6^{+1.2}_{-1.4}$)	$11.9^{+2.1}_{-2.6}$ ($12.0^{+2.1}_{-2.7}$)	$17.2^{+3.5}_{-3.2}$ ($18.2^{+3.6}_{-3.5}$)
J2323+1405	$2.9^{+1.2}_{-0.8}$ ($7.0^{+1.3}_{-1.4}$)	$12.3^{+2.4}_{-2.6}$ ($12.7^{+2.4}_{-2.6}$)	$15.4^{+3.3}_{-3.0}$ ($19.8^{+3.9}_{-3.8}$)

NOTE. — Column 2: absorbed (and unabsorbed) soft X-ray 0.5-2 keV luminosity. Column 3: absorbed (and unabsorbed) hard X-ray 2-10 keV luminosity. Column 4: absorbed (and unabsorbed) total X-ray 0.5-10 keV luminosity.

ies and [O II] $\lambda\lambda 3725, 3727$ and $H\delta$ for the $0.09 < z < 0.12$ galaxies. The F606W observations covered $H\beta$, [O III] $\lambda\lambda 4959, 5007$; [O I] $\lambda\lambda 6300, 6363$; [N II] $\lambda\lambda 6548, 6583$; $H\alpha$, and [S II] $\lambda\lambda 6716, 6730$ for the $0.02 < z < 0.06$ galaxies; $H\beta$, [O III] $\lambda\lambda 4959, 5007$; and [O I] $\lambda\lambda 6300, 6363$ for the $z = 0.09$ galaxy; and $H\gamma$, [O III] $\lambda 4363$, $H\beta$, [O III] $\lambda\lambda 4959, 5007$; and [O I] $\lambda\lambda 6300, 6363$ for the $z = 0.11$ galaxy. The F160W observations primarily traced the stellar continuum, although they may also have included [Fe II] $1.6436 \mu\text{m}$ emission for the $0.02 < z < 0.04$ galaxies and $\text{Pa}\beta$ emission for the $0.09 < z < 0.12$ galaxies.

To locate the stellar centroid of each galaxy, we fit a Sérsic profile (plus a fixed, uniform sky component) to each galaxy’s F160W image using GALFIT V3.0 (Peng et al. 2010). We ran each fit on a square region of projected physical size 40 kpc on each side, with the angular size scale calculated from z and assuming the cosmology stated in Section 1.

The errors returned by GALFIT are purely statistical in that they are computed directly from the variance of the input images. We note that in reality, the true radial profiles may deviate from the parametric model components used in GALFIT, particularly at large radii. We previously examined this in Comerford et al. (2015) by creating radial profiles of the Sérsic fits to merger-remnant galaxies, where we found that, even with significant residuals at large radii, the Sérsic component peaks are excellent tracers of the photometric peaks.

In our fitting procedure, we also attempted a two-Sérsic component fit (over the same fitting region) to test for the presence of secondary nuclei and/or close interacting neighbors. In these cases, we adopted the two-component model if the secondary component is detected at $> 3\sigma$ significance above the background. We found one system, SDSS J0839+4707, with a nearby neighbor galaxy. GALFIT returned the positions of the sources and their integrated magnitudes, which we used to determine the spatial separation on the sky between the two galaxies and their merger mass ratio. We approximated the merger mass ratio as the luminosity ratio of the two stellar bulges.

We also measured the centroid of emission for each galaxy, using Source Extractor (Bertin & Arnouts 1996) on the F606W images. According to the SDSS spectra, the [O III] $\lambda 5007$ emission line is the dominant line in the F606W image for each galaxy, within the central $3''$.

Therefore, the centroid of F606W emission within the central $3''$ is a proxy for the centroid of [O III] $\lambda 5007$ emission. We ran Source Extractor with a detection threshold of 5σ above the background, and the errors on the positions are statistical.

The positions of the emission centroids, as well as their separations from the stellar centroids, are shown in Table 6 and Figure 2. We determined the spatial separation errors by combining the errors on the GALFIT positions in the F160W data, the Source Extractor positions in the F606W data, and the relative astrometric uncertainties in the F160W (10 mas) and F606W observations (4 mas; Deustua 2016). The relative astrometric uncertainties dominate the errors, so that the spatial separation errors are all $0''.01$. We found that all of the spatial separations between the emission centroids and the stellar centroids are greater than 3σ in significance.

Finally, we measured the spatial separation between the X-ray AGN source and the center of the stellar bulge (Table 3). The error on each spatial separation incorporate the errors from the `beta2d` model fit to the *Chandra* data (Section 3.3), the GALFIT fit to the *HST*/F160W data, and the astrometric uncertainty (Section 3.5). The error budget is dominated by the uncertainty in aligning the *Chandra* and *HST* images, where the median astrometric uncertainty is $0''.5$. Due in part to these large astrometric uncertainties, all of the spatial separations are less than 3σ in significance.

3.5. Astrometry

To determine if any *Chandra* sources are significantly spatially offset from the stellar bulges seen in the *HST*/F160W data, we registered each pair of *HST*/F160W and *Chandra* images and estimated their relative astrometric uncertainties. Due to the small number of *Chandra*/ACIS sources and the relatively small *HST*/F160W field of view, we registered each image separately to SDSS (u, g, r, i , and z) and the 2MASS point source catalog (Cutri et al. 2003). Then, we combined the two transformations to register the *Chandra* and *HST* images.

We used `wavdetect` with a threshold of `sigthresh=10 $^{-8}$` to detect sources in *Chandra*, and Source Extractor with a threshold of 3σ to detect sources in SDSS, 2MASS, and *HST*. Then, we matched sources in each pair of images using the `xyxymatch` task in IRAF. Next, we used the `geomap` task in IRAF

TABLE 6
HST/F606W POSITIONS OF EACH SOURCE

SDSS Name	RA _{HST/F606W}	DEC _{HST/F606W}	$\Delta\theta(^{\prime\prime})^a$	Δx (kpc) ^a
J0132–1027	01:32:58.922	–10:27:07.01	0.078 ± 0.011	0.050 ± 0.007
J0839+4707	08:39:02.937	+47:07:56.02	0.193 ± 0.011	0.197 ± 0.011
J1055+1520	10:55:53.638	+15:20:27.96	0.124 ± 0.012	0.212 ± 0.020
J1117+6140	11:17:29.218	+61:40:15.31	0.179 ± 0.011	0.365 ± 0.023
J1346+5228	13:46:40.802	+52:28:36.23	0.252 ± 0.011	0.147 ± 0.006
J1654+1946	16:54:30.734	+19:46:15.48	0.152 ± 0.011	0.159 ± 0.011
J2323+1405	23:23:28.004	+14:05:30.03	0.111 ± 0.011	0.091 ± 0.009

NOTE. — Columns 2 and 3: coordinates of the peak of the emission, measured from *HST*/WFC3/F606W observations. Columns 4 and 5: angular and physical separations between the positions of the peak of the emission and the host galaxy’s stellar nucleus. All separations are $> 3\sigma$ in significance.

^a The errors are dominated by the astrometric uncertainties, which are 0′′01.

TABLE 7
ASTROMETRY MEASUREMENTS

SDSS Name	n_{CS}	n_{HS}	$\overline{\Delta X}$ (μ)	$\overline{\Delta Y}$ (μ)
J0132–1027	0,1,1,0,0,1	0,0,1,0,0,0	0.4656	0.2622
J0839+4707	2,2,2,2,1,1	0,2,2,2,2,1	0.2612	0.2607
J1055+1520	0,0,0,0,0,0	0,0,0,1,0,0	0.8382	0.8382
J1117+6140	0,1,1,1,0,0	0,1,1,1,0,0	0.5299	0.7136
J1346+5228	1,2,1,1,1,0	0,1,1,1,1,0	0.2837	0.3517
J1654+1946	0,0,1,1,0,0	1,2,3,3,2,1	0.4721	0.4375
J2323+1405	1,1,2,1,1,1	0,0,1,0,0,0	0.2035	0.2388

NOTE. — Column 2: number of sources matched between *Chandra* and SDSS *u*, *g*, *r*, *i*, *z* and 2MASS images. Column 3: number of sources matched between *HST*/F160W and SDSS *u*, *g*, *r*, *i*, *z* and 2MASS images. Columns 4 and 5: astrometric accuracy measurements based on matching these sources, in native *X* and *Y* coordinates of the *HST*/F160W image.

to calculate *X* and *Y* linear transformations for each matched pair ($X_{\text{shift},j}$, $Y_{\text{shift},j}$). We took the final linear transformations in *X* and *Y* to be the error-weighted averages, $\overline{X}_{\text{shift}} = \sum_{j=1}^n X_{\text{shift},j} \times w_{j,X}$ and $\overline{Y}_{\text{shift}} = \sum_{j=1}^n Y_{\text{shift},j} \times w_{j,Y}$, where *n* is the number of sources matched between two images and *w* is the error weighting.

For each dimension, *X* and *Y*, we combined in quadrature the errors on the *Chandra* and SDSS/2MASS source positions in each band. We repeated this procedure to determine the uncertainty of the relative astrometry for the *HST* and SDSS/2MASS images. Then, we added the relative astrometric errors between *Chandra* and SDSS/2MASS and between *HST* and SDSS/2MASS in quadrature to determine the relative astrometric errors between the *Chandra* and *HST* images. The final astrometric errors ($\overline{\Delta X}$, $\overline{\Delta Y}$) are then the error-weighted averages of these bands, shown in Table 7. These uncertainties range from 0′′2 to 0′′8, and they dominate the errors when we measure the spatial separations between sources in *Chandra* and *HST*.

4. RESULTS

4.1. The Galaxies Host Central AGNs, Where Shocks Produce Off-nuclear Peaks in Emission

We use the *Chandra* observations to pinpoint the location of the AGN in each galaxy, and we find that each AGN’s position is consistent with the host galaxy center to within 3σ (Table 3). Some of the AGNs may have small, but real, spatial offsets from the galaxy center, but the *HST*/F160W images do not show evidence of

secondary stellar cores that would accompany these offset AGNs. This leads us to conclude that each galaxy in our sample most likely hosts a central AGN, and not an offset AGN.

The emission line maps for each galaxy are probed by the *HST*/F606W observations, which are dominated by [O III] $\lambda 5007$. We find that the emission line centroids are spatially offset from the host galaxy centers by 0.05 to 0.4 kpc, and that all of the spatial separations are greater than 3σ in significance (Table 6). For the three galaxies that were also observed with Keck/OSIRIS, in all three galaxies the spatial offsets of the emission in the OSIRIS data are consistent with those measured in the F606W data.

Such spatially-offset peaks in emission could be produced by photoionization of an off-nuclear cloud of gas. Outflows and inflows can drive gas into off-nuclear dense regions, but this gas need not necessarily be excited by shocks (e.g., Rosario et al. 2004, 2010b). Spatially-offset peaks in emission can also be a signature of shocks. Interacting gas clouds shock the gas, enhancing the ionized gas emission and producing an off-nuclear peak of emission within the narrow line region (e.g., Mazzalay et al. 2013).

To search for further evidence of shocks, we examine the optical line flux ratios [O III] $\lambda 4363$ /[O III] $\lambda 5007$, [O III] $\lambda 5007$ /H β , and [O I] $\lambda 6300$ /[O III] $\lambda 5007$ measured from the SDSS spectrum of each galaxy. Shocks driven into the surrounding gas clouds compress the gas, increasing its density and temperature. The [O III] $\lambda 4363$ emission line indicates a very high kinetic temperature, which is produced by shock wave excitation and is inconsistent with photoionized low-density clouds. Consequently, the [O III] $\lambda 4363$ /[O III] $\lambda 5007$ line ratio is temperature sensitive and a good indicator of shock activity. Shock heating can also be probed by the [O III] $\lambda 5007$ /H β line flux ratio (e.g., Shull & McKee 1979). The [O I] $\lambda 6300$ emission line is another indicator of shocks (e.g., Dopita 1976), and [O I] $\lambda 6300$ /[O III] $\lambda 5007$ is an ionization level-sensitive line flux ratio.

We compare the [O III] $\lambda 5007$ /H β vs. [O III] $\lambda 4363$ /[O III] $\lambda 5007$ line flux ratios, as well as the [O I] $\lambda 6300$ /[O III] $\lambda 5007$ vs. [O III] $\lambda 4363$ /[O III] $\lambda 5007$ line flux ratios, to models of pure AGN photoionization and combined AGN photoionization and shocks (Moy & Rocca-Volmerange 2002). The pure photoionization models are computed with CLOUDY (Ferland 1996)

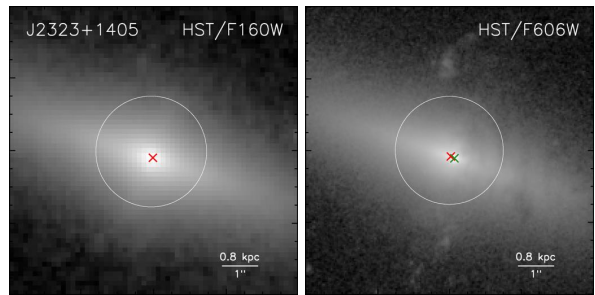
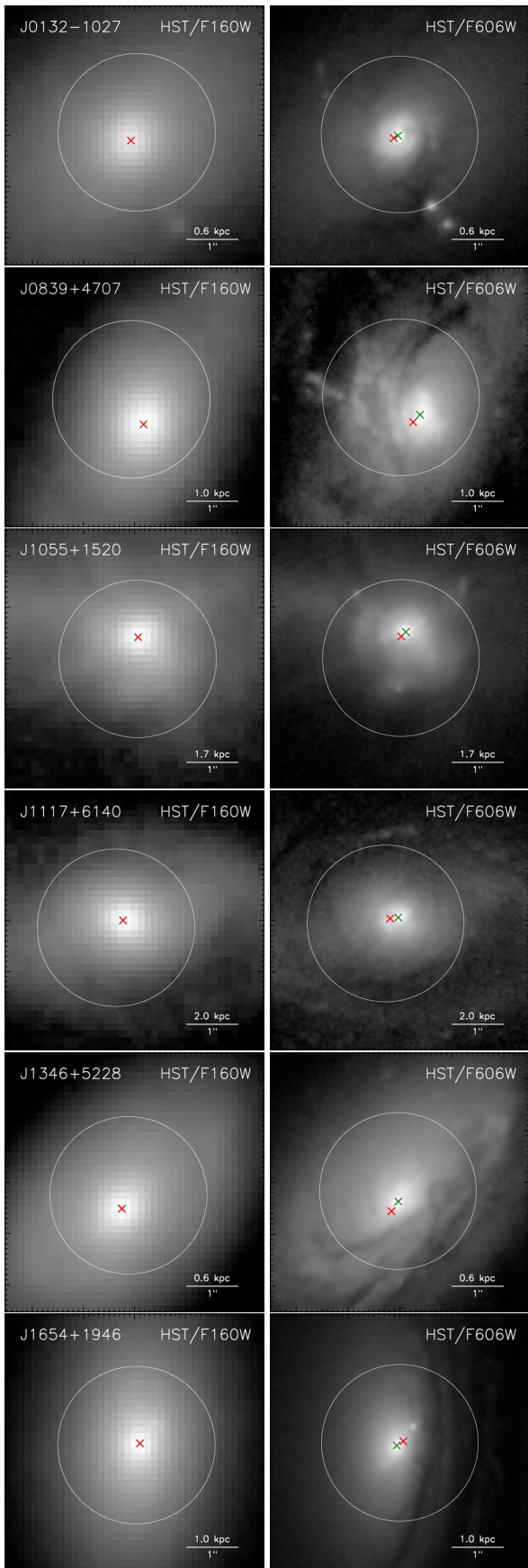


FIG. 2.— *HST*/F160W (left) and *HST*/F606W (right) images of each galaxy. The white circle illustrates the SDSS fiber, the red cross shows the galaxy’s stellar centroid based on *HST*/F160W observations, and the green cross shows the centroid of the emission source detected in the *HST*/F606W observations. All images are $5'' \times 5''$, except for the J2323+1405 images, which are $8'' \times 8''$. In all panels, north is up and east is to the left.

and use a spectral index $\alpha = -1$ of the ionizing continuum and an ionization parameter ranging from $-4 \leq \log U \leq -1$. The hydrogen density is 100 cm^{-3} , which is typical for extended emission line regions (McCarthy et al. 1990), and the metallicity is solar. The shock models are computed with MAPPINGSIII (Dopita & Sutherland 1996), and have a range of shock velocities $100 < v_s (\text{km s}^{-1}) < 1000$. We find that none of the velocity-offset AGNs have line flux ratios consistent with pure photoionization, and that instead their spectra are explained by a combination of photoionization and shocks (Figure 3).

To further explore the role of photoionization and shocks in these galaxies, we compare our data to the radiative shock models of Allen et al. (2008). They assume solar abundance, a preshock density 1 cm^{-3} , magnetic parameters ranging from 10^{-4} to $10 \mu\text{G cm}^{3/2}$, and shock velocities ranging from 200 to 1000 km s^{-1} , and they use MAPPINGSIII to model both the shock and its photoionized precursor. For shocks with velocities $\gtrsim 170 \text{ km s}^{-1}$, the ionizing front is moving faster than the shock itself, and the ionizing front dissociates and spreads out to form a precursor H II region in front of the shock. Hence, a shocked region can have both shocked gas and photoionized gas. We find that the line flux ratios of our seven velocity-offset AGNs are consistent with the shock plus precursor models of Allen et al. (2008).

We conclude that all seven of the galaxies host both shocked gas and photoionized gas. In the three galaxies observed with Keck/OSIRIS, the OSIRIS data show that the velocity-offset emission lines in the SDSS integrated spectra originate from the shocked off-nuclear emission peak in the gas (Müller-Sánchez et al. 2016). The same is most likely true for the other four galaxies in our sample, and spatially resolved spectra would show it definitively.

4.2. Sources of the Shocks in the Galaxies

Here we explore the nature of the shocks in each of the seven galaxies individually.

4.2.1. Four AGN Outflows

SDSS J0132–1027. This galaxy displays several colinear knots of emission (Figure 2), which are often seen in radio jets driving collimated AGN outflows (e.g., Middelberg et al. 2004; Rosario et al. 2010a; Tombesi et al. 2012). Indeed, SDSS J0132–1027 is detected in

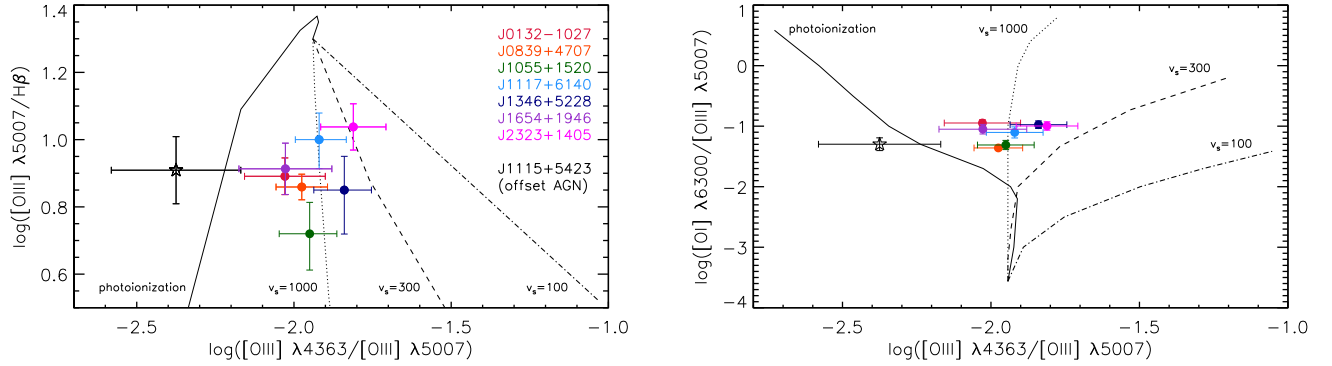


FIG. 3.— Optical line flux ratios for the seven velocity-offset AGNs in this paper (filled colored circles), and a velocity-offset AGN that is an offset AGN (open black star). Left: $[\text{O III}] \lambda 5007/\text{H}\beta$ vs. $[\text{O III}] \lambda 4363/[\text{O III}] \lambda 5007$, right: $[\text{O I}] \lambda 6300/[\text{O III}] \lambda 5007$ vs. $[\text{O III}] \lambda 4363/[\text{O III}] \lambda 5007$. The lines illustrate photoionization and shock models from Moy & Rocca-Volmerange (2002): pure photoionization models (solid line, where the ionization parameter varies from $\log U = -4$ at the bottom to $\log U = -1$ at the top), and photoionization plus shock models with shock velocities $v_s = 1000 \text{ km s}^{-1}$ (dotted line), $v_s = 300 \text{ km s}^{-1}$ (dashed line), and $v_s = 100 \text{ km s}^{-1}$ (dot-dashed line). The offset AGN’s emission lines are consistent with pure photoionization models, whereas the other velocity-offset AGNs (which do not have offset AGNs) have contributions from shocks.

the FIRST radio survey (Becker et al. 1995) with a 20 cm flux density of 1.6 mJy, and higher resolution radio observations would reveal whether it hosts a radio jet. We also note that the southwestern most knot is also detected in the F160W observations. While it is possible that this is the stellar bulge of a minor merger, it seems an unlikely coincidence that the minor merger would be colinear with the other knots of emission. Instead, the F160W observations may be tracing $[\text{Fe II}] 1.6436 \mu\text{m}$ emission, which is a common indicator of shocks (e.g., Alonso-Herrero et al. 1997) and could be produced as the jet drives into the interstellar medium.

SDSS J1055+1520. The outflow in this galaxy has been modeled as a bicone using the Keck/OSIRIS observations of $\text{Pa}\alpha$, and the ratio of the outflow energy to the AGN bolometric luminosity was found to be $\dot{E}_{\text{out}}/L_{\text{bol}} = 0.06 \pm 0.015$ (Müller-Sánchez et al. 2016). This exceeds the energy threshold for an outflow to drive a powerful two-stage feedback process that removes cold molecular gas from the inner parts of a galaxy and suppresses star formation, as found by theoretical studies ($\dot{E}_{\text{out}}/L_{\text{bol}} > 0.005$; Hopkins & Elvis 2010). Further, the bicone is oriented with a position angle $138^\circ \pm 6^\circ$ east of north, which is consistent with the spatial orientation of the X-rays (Figure 1). This hints that there may be spatially extended X-ray emission associated with the spatially extended ionized gas, and deeper X-ray observations would be required to confirm this. SDSS J1055+1520 is not detected in FIRST, so its outflow is not radio jet driven. The *HST* image also shows that the galaxy itself is asymmetric, which suggests that it may be a merger-remnant galaxy (Figure 1).

SDSS J1346+5228. This galaxy’s outflow was modeled as a bicone with the Keck/OSIRIS observations, and it is energetic enough ($\dot{E}_{\text{out}}/L_{\text{bol}} = 0.01 \pm 0.002$; Müller-Sánchez et al. 2016) to suppress star formation in the galaxy (as was also the case for SDSS J1055+1520, above). SDSS J1346+5228 is also detected in FIRST with a 20 cm flux density of 1.1 mJy, indicating that there may be a radio jet powering the outflow.

SDSS J2323+1405. This galaxy has symmetric emission line gas extending north and south of the galaxy center, out of the plane of the galaxy (Figure 2). This morphology is typical of AGN outflows (e.g., Mulchaey et al. 1996; Schmitt et al. 2003), and we conclude that SDSS J2323+1405 most likely hosts an AGN outflow.

4.2.2. Two Inflows of Gas along a Bar

SDSS J0839+4707. This galaxy has a stellar bar that is visible in Figure 1, and the peak of emission is spatially offset along the bar (Figure 2). SDSS J0839+4707 is also the only galaxy in our sample that has a close companion. The companion galaxy, SDSS J083902.50+470813.9, is located 18.8 kpc ($18''4$) to the northwest and has a redshift of $z = 0.053454 \pm 0.000045$ (Figure 4). This corresponds to a velocity difference of $311.9 \pm 21.4 \text{ km s}^{-1}$ redshifted away from the primary galaxy. Emission line diagnostics of the companion’s SDSS spectrum show that it is a star-forming galaxy (Brinchmann et al. 2004). Using the ratio of the stellar bulge luminosities as a proxy for the merger mass ratio, the merger ratio is 3.59:1 (SDSS J0839+4707 is the more massive galaxy). There is no morphological evidence that SDSS J0839+4707 and its companion are interacting, though a future interaction may trigger new accretion onto the central AGN.

SDSS J1117+6140. The OSIRIS observations of this galaxy reveal two kinematic components: a disturbed rotating disk on large scales and a counterrotating nuclear disk on the small scales of the central kpc (Müller-Sánchez et al. 2016). The galaxy’s stellar bar is apparent in Figure 1, and the peak of emission is spatially offset along the bar (Figure 2). Based on the model of the counterrotating disk (Müller-Sánchez et al. 2016), the emission peak is located where the nuclear disk and the bar intersect.

4.2.3. One Ambiguous System

SDSS J1654+1946. The *HST* observations of this galaxy show no obvious signatures of an outflow, a bar, or a merger. There is a knot of emission northwest of

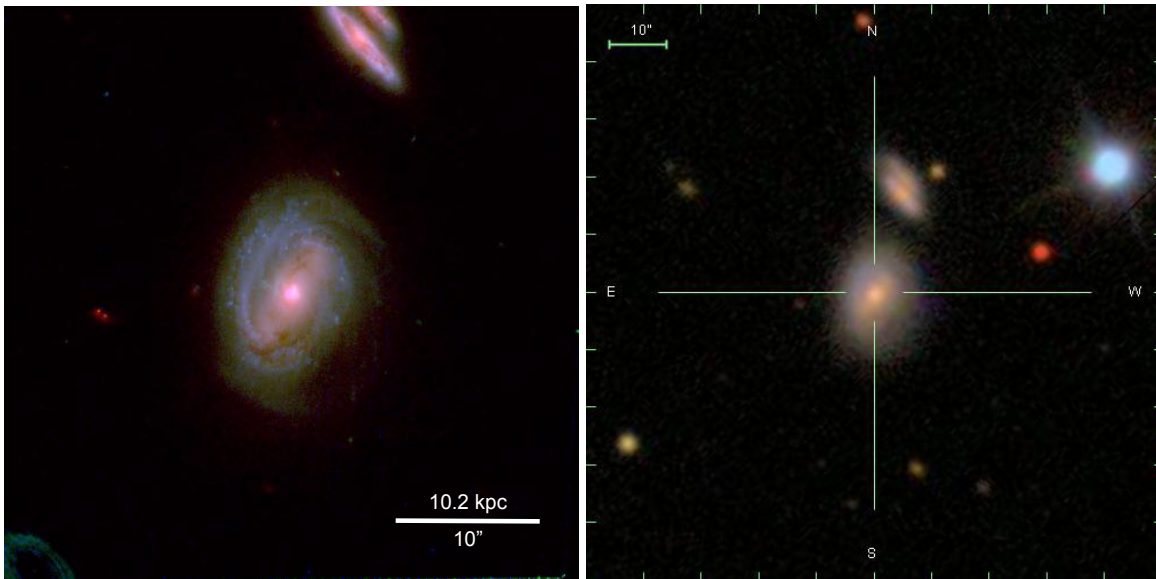


FIG. 4.— Images of the galactic environment of SDSS J0839+4707. Left: $40'' \times 40''$ four-color image of *HST* F160W (red), F606W (green), F438W (blue), and *Chandra* restframe 0.5–10 keV (purple, one-twelfth size pixels smoothed with a 16 pixel radius Gaussian kernel) observations. The *HST* and *Chandra* images have been aligned using the astrometric shifts described in Section 3.5. Right: $100'' \times 100''$ SDSS *gri* color composite image. In both panels, north is up and east is to the left.

the galaxy center (Figure 2), which could be a nuclear star cluster (e.g., Georgiev & Böker 2014). Since SDSS J1654+1946 is highly inclined (almost edge-on), we hypothesize that there could be a small nuclear bar that is too inclined to clearly see in the *HST* data. Gas inflowing along this bar could be the cause of the off-nuclear peak in emission, though without evidence of this bar we classify this system as ambiguous.

4.3. Distinguishing between Velocity Offsets Produced by Shocks and by Offset AGNs

We have determined that the velocity offsets in our seven targets are produced by shocks and not offset AGNs. Now, for comparison, we consider a velocity-offset AGN that has been confirmed as an offset AGN: SDSS J111519.98+542316.65. SDSS J1115+5423 is $z = 0.07$ galaxy that is in the velocity-offset AGN catalog (Comerford & Greene 2014) from which we selected the seven targets in this paper, and it is the only galaxy in that catalog that has been shown to be an offset AGN so far. The emission lines in SDSS J1115+5423 are offset -68.5 ± 11.9 km s $^{-1}$ from systemic. By analyzing archival *Chandra* observations of this galaxy, Barrows et al. (2016) found that it has a hard X-ray source with $L_{2-10\text{keV}} = 4 \times 10^{43}$ erg s $^{-1}$ that is located 0.8 ± 0.1 kpc ($0''.64 \pm 0''.05$) from the host galaxy center. This offset AGN is located within the $3''$ SDSS fiber and presumably is the source of the velocity-offset emission lines in the SDSS spectrum, which could be confirmed with a spatially resolved spectrum of the system.

Interestingly, SDSS J1115+5423's $[\text{O III}] \lambda 5007/\text{H}\beta$ vs. $[\text{O III}] \lambda 4363/[\text{O III}] \lambda 5007$ line flux ratios, as well as its $[\text{O I}] \lambda 6300/[\text{O III}] \lambda 5007$ vs. $[\text{O III}] \lambda 4363/[\text{O III}] \lambda 5007$ line flux ratios, are consistent with models of pure photoionization, in contrast to the seven velocity-offset AGNs studied here (Figure 3). In the case of the offset AGN (SDSS J1115+5423), the emission lines are produced by photoionization from an

AGN that is off-nuclear from the galaxy center but still within the SDSS fiber; this explains the velocity-offset emission lines observed in the SDSS spectrum. On the other hand, in each of the seven velocity-offset AGNs studied here, the emission lines originate from a *central* (not offset) AGN. Inflowing or outflowing gas is shocked, producing off-nuclear peaks in emission (still within the SDSS fiber) that result in the velocity-offset emission lines in the SDSS spectrum.

Consequently, we suggest that it is possible to separate a sample of velocity-offset AGNs into offset AGNs and central AGNs (which have shocks resulting from inflows or outflows of gas) using the shocks vs. photoionization diagnostic line flux ratios $[\text{O III}] \lambda 5007/\text{H}\beta$ vs. $[\text{O III}] \lambda 4363/[\text{O III}] \lambda 5007$, or $[\text{O I}] \lambda 6300/[\text{O III}] \lambda 5007$ vs. $[\text{O III}] \lambda 4363/[\text{O III}] \lambda 5007$. These line flux ratios are measurable with the SDSS spectrum alone; no follow-up observations are required.

5. CONCLUSIONS

We have presented *Chandra* and multiband *HST* observations of seven velocity-offset AGNs. The seven AGNs are at $z < 0.12$ and have SDSS spectra that show emission lines that are offset in line-of-sight velocity from systemic by 50 to 113 km s $^{-1}$. To determine the nature of the velocity offset in each galaxy, we use the *Chandra* observations to determine the location of the AGN and the *HST* observations to identify the galaxy's stellar centroid and the location of the peak of the ionized gas emission. Our main results are summarized as follows.

1. All seven velocity-offset AGNs have central AGNs, yet each galaxy's peak in emission is spatially offset from the stellar centroid. The spatial offsets range from 0.05 to 0.4 kpc, and they are all $> 3\sigma$ in significance. The spatially offset emission is produced by shocks, and the velocity offsets of the emission lines observed in the SDSS spectra originate from the spatially offset, shocked emission.

2. The shocks are produced by gas falling onto the AGN along a bar, or by AGN outflows propelling outward into the interstellar medium. The seven velocity-offset AGNs are classified as follows: four outflows, two inflows of gas along a bar, and one ambiguous case (since this galaxy is nearly edge-on, it may have a bar that is difficult to see).

3. All of the velocity-offset AGNs studied here fall in the regions of the [O III] $\lambda 5007/H\beta$ vs. [O III] $\lambda 4363/[O III] \lambda 5007$ and [O I] $\lambda 6300/[O III] \lambda 5007$ vs. [O III] $\lambda 4363/[O III] \lambda 5007$ diagrams that are consistent with a combination of photoionization and shock contributors. However, a comparison velocity-offset AGN (where the velocity offset is caused by an offset AGN in a galaxy merger) is consistent with models of pure photoionization and no shocks. We suggest that these emission lines, measured from the SDSS spectrum alone, may efficiently separate the velocity-offset AGNs produced by offset AGNs (photoionization only) from those produced by central AGNs with shocked gas in inflows or outflows (photoionization plus shocks).

Additional follow-up observations, including spatially resolved spectroscopy, X-ray observations, and radio observations, of a large sample of velocity-offset AGNs could test the hypothesis that the [O III] $\lambda 5007/H\beta$, [O III] $\lambda 4363/[O III] \lambda 5007$, and [O I] $\lambda 6300/[O III] \lambda 5007$ line flux ratios distinguish the offset AGNs from the central AGNs with shocks. The offset AGNs could then be used for studies of AGN fueling during galaxy mergers (e.g., Barrows et al. 2017), while the central AGNs with outflows may be particularly effective drivers of feedback. Since the outflows selected from velocity-offset AGNs are outflows *with*

shocks, these outflows have already been pre-selected to be interacting with their host galaxies. In fact, we found that the two outflows in our sample that were modeled as bicones are energetic enough to drive cold molecular gas out of the galaxy's inner regions and regulate star formation. Thus, AGN outflows with velocity offsets may be a rich source of examples of feedback.

We thank the anonymous referee for comments that have improved the clarity of this paper. Support for this work was provided by NASA through Chandra Award Number GO4-15113X issued by the Chandra X-ray Observatory Center, which is operated by the Smithsonian Astrophysical Observatory for and on behalf of NASA under contract NAS8-03060. Support for HST program number GO-13513 was provided by NASA through a grant from the Space Telescope Science Institute, which is operated by the Association of Universities for Research in Astronomy, Inc., under NASA contract NAS5-26555.

The scientific results reported in this article are based in part on observations made by the Chandra X-ray Observatory, and this research has made use of software provided by the Chandra X-ray Center in the application packages CIAO, ChIPS, and Sherpa. The results reported here are also based on observations made with the NASA/ESA Hubble Space Telescope, obtained at the Space Telescope Science Institute, which is operated by the Association of Universities for Research in Astronomy, Inc., under NASA contract NAS 5-26555. These observations are associated with program number GO-13513.

Facilities: CXO, HST

REFERENCES

- Allen, J. T., Schaefer, A. L., Scott, N., Fogarty, L. M. R., Ho, I.-T., Medling, A. M., Leslie, S. K., Bland-Hawthorn, J., Bryant, J. J., Croom, S. M., Goodwin, M., Green, A. W., Konstantopoulos, I. S., Lawrence, J. S., Owers, M. S., Richards, S. N., & Sharp, R. 2015, *MNRAS*, 451, 2780
- Allen, M. G., Groves, B. A., Dopita, M. A., Sutherland, R. S., & Kewley, L. J. 2008, *ApJS*, 178, 20
- Alonso-Herrero, A., Rieke, M. J., Rieke, G. H., & Ruiz, M. 1997, *ApJ*, 482, 747
- Barrows, R. S., Comerford, J. M., Greene, J. E., & Pooley, D. 2016, *ApJ*, 829, 37
- . 2017, *ApJ*, 838, 129
- Barrows, R. S., Sandberg Lacy, C. H., Kennefick, J., Comerford, J. M., Kennefick, D., & Berrier, J. C. 2013, *ApJ*, 769, 95
- Barrows, R. S., Stern, D., Madsen, K., Harrison, F., Assef, R. J., Comerford, J. M., Cushing, M. C., Fassnacht, C. D., Gonzalez, A. H., Griffith, R., Hickox, R., Kirkpatrick, J. D., & Lagattuta, D. J. 2012, *ApJ*, 744, 7
- Becker, R. H., White, R. L., & Helfand, D. J. 1995, *ApJ*, 450, 559
- Bertin, E., & Arnouts, S. 1996, *A&AS*, 117, 393
- Bevington, P. R. 1969, *Data reduction and error analysis for the physical sciences*
- Blecha, L., Loeb, A., & Narayan, R. 2013, *MNRAS*, 429, 2594
- Brinchmann, J., Charlot, S., White, S. D. M., Tremonti, C., Kauffmann, G., Heckman, T., & Brinkmann, J. 2004, *MNRAS*, 351, 1151
- Comerford, J. M., Gerke, B. F., Newman, J. A., Davis, M., Yan, R., Cooper, M. C., Faber, S. M., Koo, D. C., Coil, A. L., Rosario, D. J., & Dutton, A. A. 2009, *ApJ*, 698, 956
- Comerford, J. M., Gerke, B. F., Stern, D., Cooper, M. C., Weiner, B. J., Newman, J. A., Madsen, K., & Barrows, R. S. 2012, *ApJ*, 753, 42
- Comerford, J. M., & Greene, J. E. 2014, *ApJ*, 789, 112
- Comerford, J. M., Pooley, D., Barrows, R. S., Greene, J. E., Zakamska, N. L., Madejski, G. M., & Cooper, M. C. 2015, *ApJ*, 806, 219
- Comerford, J. M., Pooley, D., Gerke, B. F., & Madejski, G. M. 2011, *ApJ*, 737, L19+
- Comerford, J. M., Schluns, K., Greene, J. E., & Cool, R. J. 2013, *ApJ*, 777, 64
- Croton, D. J., Springel, V., White, S. D. M., De Lucia, G., Frenk, C. S., Gao, L., Jenkins, A., Kauffmann, G., Navarro, J. F., & Yoshida, N. 2006, *MNRAS*, 365, 11
- Cutri, R. M., Skrutskie, M. F., van Dyk, S., Beichman, C. A., Carpenter, J. M., Chester, T., Cambresy, L., Evans, T., Fowler, J., Gizis, J., Howard, E., Huchra, J., Jarrett, T., Kopan, E. L., Kirkpatrick, J. D., Light, R. M., Marsh, K. A., McCallon, H., Schneider, S., Stiening, R., Sykes, M., Weinberg, M., Wheaton, W. A., Wheelock, S., & Zacarias, N. 2003, *VizieR Online Data Catalog*, 2246
- Deustua, S. 2016
- Di Matteo, T., Springel, V., & Hernquist, L. 2005, *Nature*, 433, 604
- Dickey, J. M., & Lockman, F. J. 1990, *ARA&A*, 28, 215
- Dopita, M. A. 1976, *ApJ*, 209, 395
- Dopita, M. A., & Sutherland, R. S. 1996, *ApJS*, 102, 161
- Fabian, A. C. 2012, *ARA&A*, 50, 455
- Ferland, G. J. 1996, *Hazy, A Brief Introduction to Cloudy 90*
- Fu, H., Yan, L., Myers, A. D., Stockton, A., Djorgovski, S. G., Aldering, G., & Rich, J. A. 2012, *ApJ*, 745, 67
- Fu, H., Zhang, Z.-Y., Assef, R. J., Stockton, A., Myers, A. D., Yan, L., Djorgovski, S. G., Wrobel, J. M., & Riechers, D. A. 2011, *ApJ*, 740, L44+
- Georgiev, I. Y., & Böker, T. 2014, *MNRAS*, 441, 3570
- Greene, J. E., Zakamska, N. L., & Smith, P. S. 2012, *ApJ*, 746, 86
- Heckman, T. M., & Best, P. N. 2014, *ARA&A*, 52, 589
- Heckman, T. M., Ptak, A., Hornschemeier, A., & Kauffmann, G. 2005, *ApJ*, 634, 161
- Hopkins, P. F., & Elvis, M. 2010, *MNRAS*, 401, 7
- Ishibashi, W., & Courvoisier, T.-L. 2010, *Astronomy & Astrophysics*, 512, A58
- Lagarias, J. C., Reeds, J. A., Wright, M. H., & Wright, P. E. 1998, *SIAM Journal on optimization*, 9, 112
- Liu, X., Civano, F., Shen, Y., Green, P., Greene, J. E., & Strauss, M. A. 2013, *ApJ*, 762, 110

- Liu, X., Shen, Y., Strauss, M. A., & Greene, J. E. 2010, *ApJ*, 708, 427
- Mazzalay, X., Rodríguez-Ardila, A., Komossa, S., & McGregor, P. J. 2013, *MNRAS*, 430, 2411
- McCarthy, P. J., Spinrad, H., Dickinson, M., van Breugel, W., Liebert, J., Djorgovski, S., & Eisenhardt, P. 1990, *ApJ*, 365, 487
- McGurk, R. C., Max, C. E., Medling, A. M., Shields, G. A., & Comerford, J. M. 2015, *ApJ*, 811, 14
- Middelberg, E., Roy, A. L., Nagar, N. M., Krichbaum, T. P., Norris, R. P., Wilson, A. S., Falcke, H., Colbert, E. J. M., Witzel, A., & Fricke, K. J. 2004, *A&A*, 417, 925
- Moy, E., & Rocca-Volmerange, B. 2002, *A&A*, 383, 46
- Mulchaey, J. S., Wilson, A. S., & Tsvetanov, Z. 1996, *ApJS*, 102, 309
- Müller-Sánchez, F., Comerford, J., Stern, D., & Harrison, F. A. 2016, *ApJ*, 830, 50
- Müller-Sánchez, F., Comerford, J. M., Nevin, R., Barrows, R. S., Cooper, M. C., & Greene, J. E. 2015, *ApJ*, 813, 103
- Nandra, K., & Pounds, K. A. 1994, *MNRAS*, 268, 405
- Nevin, R., Comerford, J., Müller-Sánchez, F., Barrows, R., & Cooper, M. 2016, *ApJ*, 832, 67
- Oh, K., Sarzi, M., Schawinski, K., & Yi, S. K. 2011, *ApJS*, 195, 13
- Park, T., Kashyap, V. L., Siemiginowska, A., van Dyk, D. A., Zezas, A., Heinke, C., & Wargelin, B. J. 2006, *ApJ*, 652, 610
- Peng, C. Y., Ho, L. C., Impey, C. D., & Rix, H.-W. 2010, *AJ*, 139, 2097
- Piconcelli, E., Jimenez-Bailón, E., Guainazzi, M., Schartel, N., Rodríguez-Pascual, P. M., & Santos-Lleó, M. 2005, *A&A*, 432, 15
- Reeves, J. N., & Turner, M. J. L. 2000, *MNRAS*, 316, 234
- Rosario, D. J., Shields, G. A., Taylor, G. B., Salviander, S., & Smith, K. L. 2010a, *ApJ*, 716, 131
- Rosario, D. J., Whittle, M., Nelson, C. H., & Wilson, A. S. 2010b, *MNRAS*, 408, 565
- Rosario, D. J., Whittle, M., Silverman, J. D., Wilson, A. S., & Nelson, C. H. 2004, in *IAU Symposium*, Vol. 222, *The Interplay Among Black Holes, Stars and ISM in Galactic Nuclei*, ed. T. Storchi-Bergmann, L. C. Ho, & H. R. Schmitt, 287–290
- Schmitt, H. R., Donley, J. L., Antonucci, R. R. J., Hutchings, J. B., & Kinney, A. L. 2003, *ApJS*, 148, 327
- Shull, J. M., & McKee, C. F. 1979, *ApJ*, 227, 131
- Steinborn, L. K., Dolag, K., Comerford, J. M., Hirschmann, M., Remus, R.-S., & Teklu, A. F. 2016, *MNRAS*, 458, 1013
- Tombesi, F., Sambruna, R. M., Marscher, A. P., Jorstad, S. G., Reynolds, C. S., & Markowitz, A. 2012, *MNRAS*, 424, 754